Additive Manufacturing 44 (2021) 102036

Contents lists available at ScienceDirect

Additive Manufacturing

journal homepage: www.elsevier.com/locate/addma

Research Paper

Influence of friction stir processing and aging heat treatment on microstructure and mechanical properties of selective laser melted Mg-Gd-Zr alloy

Qingchen Deng, Yujuan Wu *, Ning Su, Zhiyu Chang, Juan Chen, Liming Peng, Wenjiang Ding

National Engineering Research Center of Light Alloy Net Forming and State Key Laboratory of Metal Matrix Composites, School of Materials Science and Engineering, Shanghai Jiao Tong University, Shanghai 200240, China

ARTICLE INFO

Keywords:
Selective laser melting (SLM)
Mg-Gd-Zr alloy
Friction stir processing (FSP)
Microstructure
Mechanical properties

ABSTRACT

The low ductility of Mg alloy fabricated by selective laser melting (SLM) technique usually restricts its application in several fields. Friction stir processing (FSP) is a promising post-treatment method to solve this problem. A detailed study of how FSP affect pore defects, molten pool boundary, grain morphology, aging precipitates and mechanical properties of SLMed Mg-10Gd-0.2Zr (G10K, wt.%) alloy was conducted. The results show that FSP can lead to porosity reduction from 0.779% to 0.015%, vanishment of molten pool boundary, columnar to equiaxed transition and grain refinement. Thus, a significant enhancement of room temperature tensile properties is reported with a remarkable increase of elongation (EL) from 2.2% to 7.5% without the sacrifice of strength after FSP (while yield strength (YS) and ultimate tensile strength (UTS) increased from 180 MPa, 228 MPa to 202 MPa, 272 MPa respectively). After peak aging heat treatment, the plate aspect ratio and area number density of β' aging precipitates in the FSP-T5 G10K alloy are higher than those of SLM-T5 G10K alloy, resulting in a stronger aging hardening response (hardness increment 28.3 HV versus 22.7 HV). As a result, the FSP-T5 G10K alloy exhibits YS of 285 MPa, UTS of 356 MPa and EL of 1.3%, while those of the SLM-T5 G10K alloy are only 243 MPa, 260 MPa and 0.3%. These findings demonstrate that FSP is very effective for modifying microstructure and enhancing mechanical properties of the SLMed alloys.

1. Introduction

As one of the most promising metal additive manufacturing (AM) technologies, selective laser melting (SLM) has a high potential for preparing magnesium (Mg) alloy components with high-performance complex structures to replace traditional casting process [1–3]. The SLMed Mg alloys can be widely applied in automotive, space, aircraft and biomedical industries [4–6] owing to the advantages of low density, superior specific strength, outstanding biodegradability and biocompatibility, low modulus and exceptional damping capacity [7]. The scanning speed of laser beam is fast (hundreds of mm/s) and the small molten pool size (hundreds of μm), so the cooling rate of SLM process is as high as 10^5 K/s [8]. Therefore, a fine-grained microstructure was usually formed in the SLMed alloys leading to higher strength than that of the as-cast alloys [9,10]. Nevertheless, the ductility or elongation of the SLMed alloys is generally worse than that of the as-cast alloys [11–13] owing to the presence of porosity [11,14], microstructure inhomogeneity [15] caused by the difference in solidification conditions of different positions in the molten pool, residual stress [16] originating from large temperature gradient, etc.

During the SLM process, Mg evaporated very easily and produced large quantities of fumes owing to the low boiling point (~1093℃) and high saturated vapor pressure of Mg element [17]. As a result, the pore defects caused by Mg evaporation were difficult to completely eliminate by adjusting SLM processing parameters. For instance, Wei et al. [11] revealed that the optimal elongation of the SLMed AZ91D Mg alloy was only 1.83% although the relative density was as high as 99.52%. Hyer et al. [13] optimized laser power and scanning speed for WE43 Mg alloy and got a very high relative density (~99.7%), but the maximum tensile strain at fracture in the as-built condition was only 2.6%, which was still not satisfactory. In order to ameliorate the mechanical properties especially ductility of SLMed Mg alloys, appropriate post-treatment methods are urgently needed to be developed.

Post heat treatment (HT) is a common post-treatment method

* Corresponding author.
E-mail address: wuyj@sjtu.edu.cn (Y. Wu).

https://doi.org/10.1016/j.addma.2021.102036
Received 10 February 2021; Received in revised form 30 April 2021; Accepted 3 May 2021
Available online 21 May 2021
2214-8604/© 2021 Elsevier B.V. All rights reserved.

because high temperature not only promotes the release of residual stress, but also dissolves the brittle second phase into the matrix, both of which are beneficial to improve ductility. For instance, Hyer et al. [13] used HT (solid solution treated at 536°C for 24 h and then ageing treated at 205°C for 48 h) to modify the microstructure and mechanical properties of the SLMed WE43 Mg alloy, and exhibited that the fracture strain obtained a small increase from 2.6% to 4.3% after HT but the YS and UTS remained basically unchanged. The reason for the improved ductility was that the globular β_1-Mg_3Nd precipitates in the SLMed state were dissolved and re-precipitated into thin sheets after HT. Moreover, hot isostatic pressing (HIP) is another common post-treatment method, which applies high temperature and high pressure simultaneously to close internal pores of the SLMed components. And this method is usually used to improve fatigue properties by decreasing the size of defects [18]. Liu et al. [19] applied HIP (450℃, 103 MPa, 3 h) to improve defects and low plasticity in the SLMed AZ61 Mg alloy, and revealed that a majority of the pores were closed and the relative density approached 100% after HIP resulting in an increase in EL from 3.1% to 8.2% but the microhardness, YS and UTS were all decreased after HIP.

However, both post-HT and HIP share a common issue that is the drastic grain growth during high temperature process, which will adversely affect the tensile strength. Besides, the fine-grained rapid solidification non-equilibrium microstructure of the SLMed alloys has a greater tendency for the phenomenon of grain growth to occur and the increment of grain size will be higher than that of the as-cast alloys under the same temperature and time conditions [20]. Thus, new post-treatment methods need to be exploited, which can generate a homogeneous microstructure to increase EL greatly, while ensuring that the tensile strength does not drop or even rise at the same time.

As an emerging severe plastic deformation (SPD) technique, friction stir processing (FSP) is derived from the basic principle of friction stir welding (FSW), which uses the high strain, high strain rate as well as high temperature at the same time to make the material flow fully leading to grain refinement, second phase fragmentation, homogenization and densification in the stir zone [21]. It has been extensively demonstrated that FSP can produce relatively uniform microstructures and enhance mechanical properties of cast Mg alloys [22–24]. Huang et al. [25] applied FSP on the SLMed Ti6Al4V alloy to reduce the porosity and homogenize the microstructure, and exhibited that the fracture strain received a significant increase from 0.21 to 0.65 after FSP. FSP also improved ductility and fatigue life of the SLMed AlSi10Mg alloy owing to the spheroidization of the eutectic phase, the homogenization of the microstructure and the decrease of porosity [15]. However, as far as the authors know, there is no evidence reported in literature on adjusting microstructures and enhancing mechanical properties of the SLMed Mg alloys by means of FSP.

In the present study, a SLMed G10K alloy was post-treated by FSP and microstructure and mechanical properties were systematically studied before and after FSP. Besides, considering the strong precipitation hardening potential of Mg-Gd series alloys [26–28], the SLMed and FSPed alloys were subjected to artificial aging heat treatment to further raise the tensile strength especially YS and the influence of FSP on the size and area number density of β' aging precipitates was discussed.

2. Experimental details

2.1. Powder preparation

G10K alloy ingots were prepared by means of semi-continuous casting. The G10K pre-alloyed powders were supplied by Tangshan Weihao Magnesium Powder Co., LTD., China through remelting alloy ingots and subsequent centrifugal atomization process. An inductively coupled plasma atomic emission spectroscopy analyzer (ICPAES, Perkin-Elmer, Optima™ 7300 DV) was used to analyze the actual chemical compositions of the original G10K powders and the SLMed G10K alloys. The powders were first dissolved in aqua regia (a mixture of concentrated HCl and concentrated HNO_3 in a volume ratio of 3:1), then underwent atomization to disperse into small droplets, and the high temperature generated by the argon plasma finally completely decomposes the droplets to form excited atoms. Because the atoms in the excited state are unstable, the outer electrons will transition from the excited state to a lower energy level, thus emitting characteristic spectral lines. The intensity of a specific wavelength is detected to determine the content of the elements in the powders. As shown in Table 1, the content of Gd and Zr elements in the SLMed alloys was higher than that of original powders as a result of serious vaporization loss of Mg element.

Table 1
The actual chemical compositions of the original G10K powders and the SLMed G10K alloys (wt.%).

Materials	Gd	Zr	Mg
Powders	10.17 ± 0.30	0.18 ± 0.03	Bal.
SLMed alloys	12.46 ± 0.25	0.23 ± 0.01	Bal.

Fig. 1 shows the macro morphology (a), SE-SEM image (b), BSE-SEM image (c) and particle size distribution (d) of the G10K alloy powders. The G10K alloy powders were highly spherical shaped (Fig. 1a–c), which meets the requirements of SLM process. As displayed in Fig. 1c, the powders were consisted of gray α-Mg matrix and bright white eutectic phase at grain boundaries. According to the linear intercept method (the ASTM E112–12), the average grain size of the powders was 2.84 ± 0.29 μm. A sieved particle size distribution (Fig. 1d) between 46.01 μm (D10) and 84.86 μm (D90) was obtained by a laser diffraction particle size analyzer (Microtrac S3500 series). The mean particle diameter of volume was 63.85 μm.

2.2. SLM and FSP procedures

In the present research, the G10K alloy rectangular plate with a size of 120 × 50 × 4.5 mm^3 (Fig. 2a) was manufactured by SLM by using a commercial ZRapid iSLM 150 machine (ZRapid Tech Co., LTD., China). During the entire SLM process, an inert gas (high purity Ar) circulation system was applied to guarantee low oxygen and water vapor content (<100 ppm) and remove a large amount of fumes promptly created by the severe evaporation of Mg element. Based on our previous research of the SLMed Mg-Gd based alloys [9], the SLM processing parameters were as follows: the laser power was 80 W, the laser scanning speed was 200 mm/s, the hatch spacing was 100 μm, the layer thickness was 30 μm. Regarding the scanning strategy, a tape strategy with width of 5 mm was adopted and the hatch angle was 73° in order to reduce stress accumulation. Electric discharge wire cutting was employed to separate all SLMed samples from the substrate plate after SLM.

The SLMed G10K alloy plate was then friction stir processed by adopting a multiple functional friction stir welding machine. Fig. 2b exhibits a schematic diagram of the FSP process, where PD, TD and ND stand for the processing direction, the transverse direction and the normal direction (the building direction of SLM process) respectively. Two parallel passes (Fig. 2c) were performed using a rotation rate of 800 rpm and a traversing speed of 50 mm/min according to our previous study [21]. The processing tool include a shoulder (the diameter is 15 mm) and a cylinder threaded pin (the length is 3 mm and the diameter is 5 mm). The plunge depth and the tilting degree were preserved 1.25 mm and 2.5°, respectively during the whole FSP process. After FSP, the microstructural observation samples and tensile test samples (Fig. 2b) were extracted from the middle part of stir zone using electric discharge wire cutting equipment. The dimensions of SLMed and FSPed tensile test samples (Fig. 2d) were the same.

2.3. Microstructure characterization and mechanical properties analysis

The microstructure of the SLMed and FSPed G10K alloys was

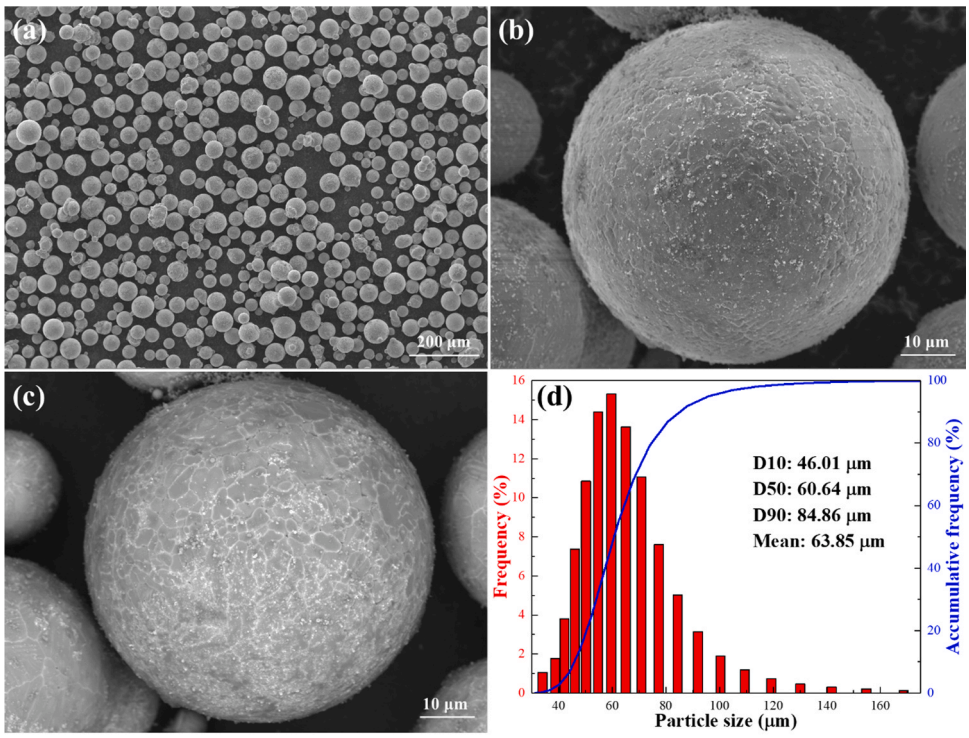

Fig. 1. The macro morphology (a), SE-SEM image (b), BSE-SEM image (c) and particle size distribution (d) of the G10K alloy powders.

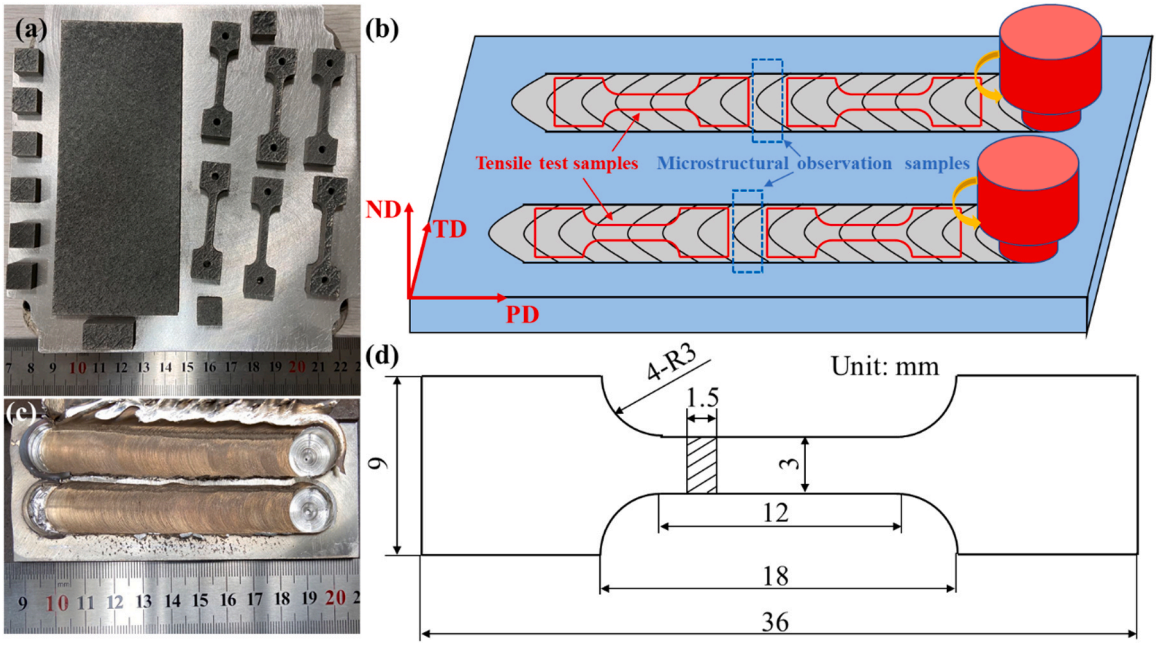

Fig. 2. (a) The top view of SLMed samples; (b) the location for microstructural observation samples and tensile test samples; (c) the top view of SLMed plate after FSP; (d) the dimensions of SLMed and FSPed tensile test samples.

investigated by optical microscope (OM, Zeiss Axio observer A1), scanning electron microscope (SEM, TESCAN MIRA3), electron back-scattering diffraction (EBSD, TESCAN GAIA3) and transmission electron microscope (TEM, FEI TECNAI G2 S-TWIN). As for the sample surface preparation procedures for OM and SEM observations, the samples were mechanically ground by SiC abrasive papers (#320, #1200, #3000, #7000) and then polished with nano magnesium oxide (≤50 nm) suspension, afterwards, first etched in the acetic-nitric-ethylene glycol solution (20 ml acetic acid, 1 ml nitric acid, 60 ml ethylene glycol and 19 ml water) for 1–2 s and then etched in the acetic-picral solution (10 ml acetic acid, 4.2 g picric acid, 70 ml ethyl alcohol and 10 ml water) for 3–5 s. The sample preparation methods for EBSD and TEM can be found in our previously published work [9]. The porosity was examined by Image Pro Plus software at least five OM images from different regions. The grain orientation maps and average grain size were acquired by the TSL OIM Analysis 7 software. The phase constitutions of the powder, SLMed and FSPed alloys were measured by X-ray diffraction (XRD, Poly-functional X-Ray Diffractometer equipped with a

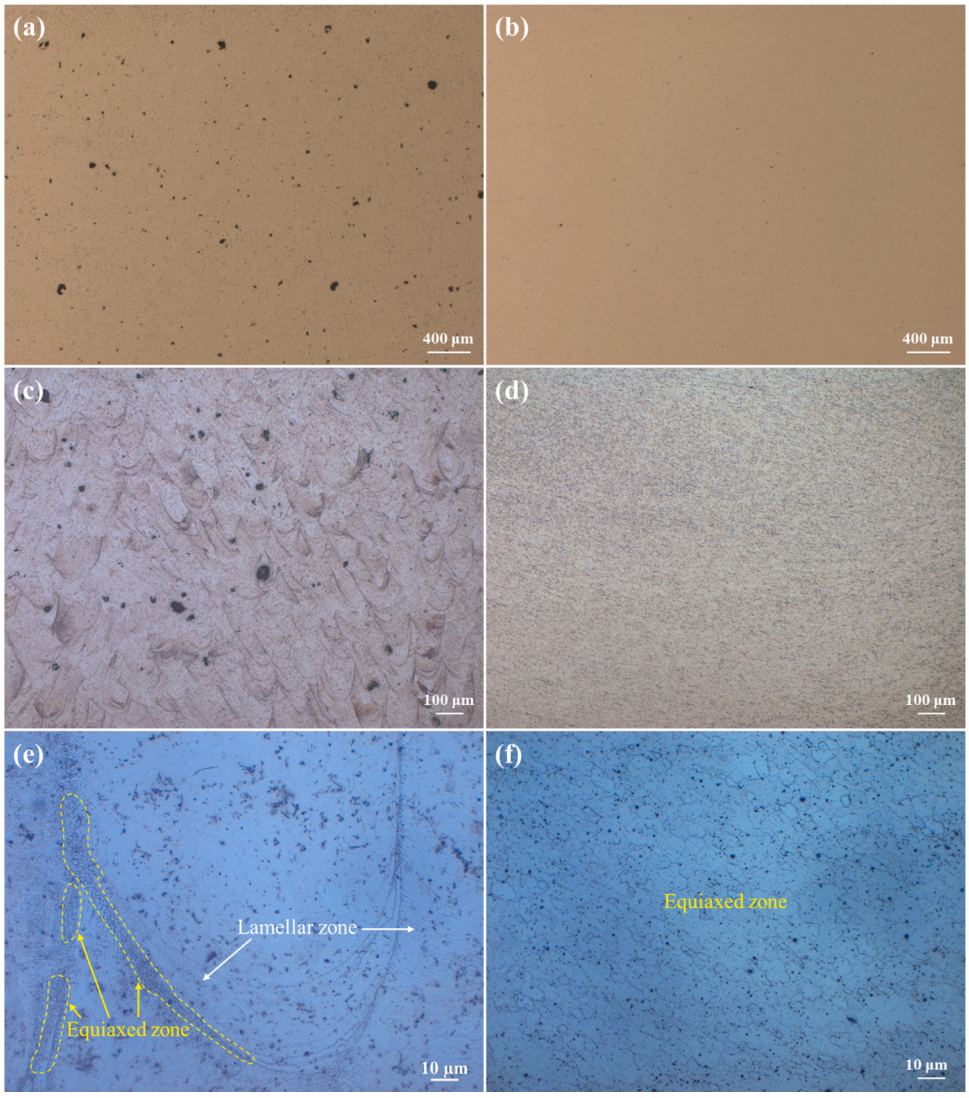

Fig. 3. OM images of SLMed (a, c, e) and FSPed (b, d, f) G10K alloy.

Cu-Kα radiation source operating at 40 kV and 40 mA), and the scanning angle ranged from 20° to 60° at a scanning speed of 1°/min.

The SLMed and FSPed samples were artificially aged at 200 ℃ in an oil bath. The aging hardening response was measured via Vickers hardness testing (the load was 49 N and the residence time was 15 s). Each Vickers hardness value at different aging time was gained from the averages of at least seven independent measurement values (minimum and maximum values were removed). Tensile tests were performed on a Zwick/Roell Z100 material testing machine and the loading speed was fixed at 0.5 mm/min. The loading direction of the tensile tests was perpendicular to the building direction (BD) of SLM process. Room temperature tensile properties including YS, UTS and EL were averaged from at least three parallel tests.

3. Results and discussion

3.1. The influence of FSP on pore defects

Fig. 3 presents the OM images of the SLMed (a, c) and FSPed (b, d) G10K alloy. There are many pores (Fig. 3a) in the SLMed G10K alloy, most of which are circular gas pores with diameter of 10–60 μm originating from the serious vaporization of Mg and a few of which are irregular pores because of the incomplete remelting of former layers. The porosity of the SLMed G10K alloy is 0.779 ± 0.090%, which is comparable to the porosity of the SLMed AZ61 Mg alloy (0.6%) [19] under the optimum processing parameters. There is no doubt that the pores in metal materials can give rise to stress concentration, thus resulting in degraded tensile strength and ductility [14]. It is difficult to fabricate a fully dense (the relative density is 100%) Mg alloy sample only by adjusting the SLM processing parameters, so post-treatment after SLM is necessary. Obviously, the pores, especially large pores disappear after FSP (Fig. 3b) and the porosity of the FSPed G10K alloy is only 0.015 ± 0.008%. Therefore, FSP can close the pre-existing pores due to the thermomechanical effect during FSP: the high temperature decreases YS of materials resulting in complex material flow and then the high shear strain in the stir zone is helpful to close pores [29].

3.2. The influence of FSP on molten pool boundary and grain morphology

Besides, as shown in Fig. 3c, fish-scale-shaped molten pools are arranged along building direction of the SLM process. The typical width and depth of molten pools are 110 μm and 60 μm respectively. However, the molten pool boundaries vanish after FSP (Fig. 3d). The SLMed alloy consists of equiaxed zone near the boundary of the molten pool and lamellar zone at the interior of the molten pool (Fig. 3e) while the FSPed alloy is completely composed of equiaxed zone (Fig. 3f). In other words, the molten pool structure and the differentiated zones of the SLMed alloy can be eliminated after FSP, thus contributing to homogenization

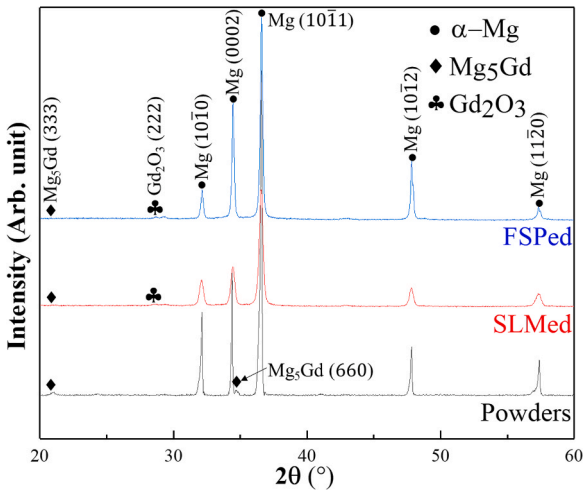

Fig. 4. XRD patterns of the powder, SLMed and FSPed G10K alloy.

effect on the mesoscopic structural scale.

The XRD patterns in Fig. 4 reveal that the powders contain two phases: α-Mg matrix and secondary eutectic phase (Mg_5Gd). After SLM and FSP process, diffraction peaks of Mg_5Gd are relatively poor compared with α-Mg suggesting that the amount of eutectic phase in SLMed and FSPed alloys is lower than that in powders. Besides, a new oxide phase (Gd_2O_3) is generated implying the slight oxidation during SLM.

Furthermore, all the phases of the SLMed and FSPed G10K alloys are evidently examined in the BSE-SEM micrographs shown in Fig. 5. The cooling rate is highest at the molten pool boundaries, thus resulting in extremely fine equiaxed grains (~2 μm) [30]. At the interior of the molten pool, the lamellae with width of about 0.7 μm are separated by lines of Gd-rich secondary eutectic phase and adjacent lamellae are parallel to each other indicating similar crystallographic orientation (Fig. 5a), which is similar to those in the SLMed WE43 Mg alloy [31].

The lamellae are often observed in eutectic alloys while the chemical composition of G10K is far from the eutectic points (36.9 wt.%) of binary Mg-Gd system. Hexagonal dendrites usually form during the solidification of Mg alloys and the lamellae may be formed when a specific growth direction of Mg dendrites is advantageous. The preferential growth of Mg dendrites leads to lined-up dendrite trunks on specific direction. The limited growth between lamellae forms an inter-dendritic liquid greatly enrich in Gd solute element, whose chemical composition approaches the eutectic points of binary Mg-Gd system. The eutectic phase mixture including Mg and Gd-rich secondary eutectic phase solidifies and generates lamellae boundaries when the liquid temperature drops to the eutectic temperature. Based on EBSD orientation map of SLMed G10K alloy (Fig. 7a), the lamellae boundaries in Fig. 5a and b are not grain boundaries, which is very unique due to rapid non-equilibrium solidification and complicated thermal history of SLM. Compared with coarse net-like eutectic phase and large grains in as-cast Mg-Gd series alloys [32–34], the SLMed alloy contains lesser and thinner Mg_5Gd eutectic phase and smaller grain size owing to rapid solidification. Fig. 6 reveals that the flaky white particles are rich in Gd and O elements, indicating the presence of randomly distributed gadolinium oxide particles as the affinity of the rare earth Gd element to O is greater than that of Mg, which originate from the oxide shell of original powders [10,13] and residual oxygen in the process atmosphere. The oxide particles are detrimental to mechanical properties owing to the undesirable interface combination, which are usually named oxide inclusions in cast alloys. The lamellae disappear and a fully equiaxed microstructure is formed after FSP (Fig. 5c and d). Besides, the number of oxide particles decreases and the size becomes smaller after FSP, which is conducive to the increase of EL. For one thing the eutectic phase is dissolved into α-Mg matrix due to the high temperature during FSP. For another there will be many fine dot-like Mg_5Gd phases (tens of nanometers) precipitated from α-Mg matrix during cooling process. In summary, the stripped eutectic phase in the SLMed alloy is markedly broken into fine and dispersed phase after FSP, which is expected to improve tensile strength and ductility simultaneously.

Since the grain boundaries at the interior of the molten pool are not obvious, EBSD test was employed to identify the morphology and size of

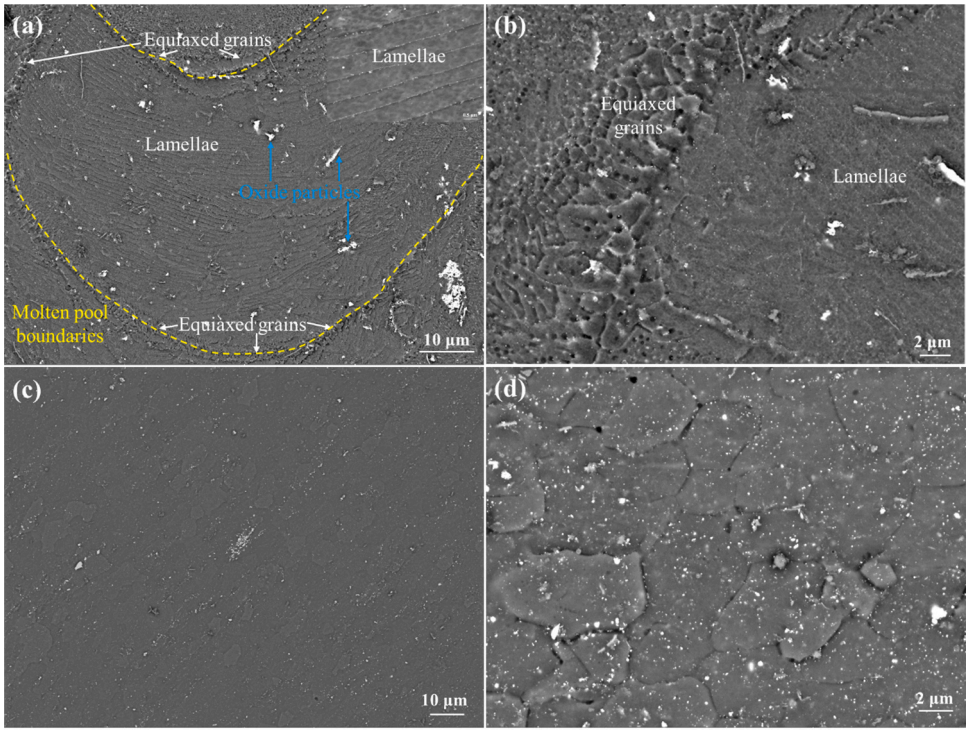

Fig. 5. BSE-SEM micrographs of SLMed (a, b) and FSPed (c, d) G10K alloy.

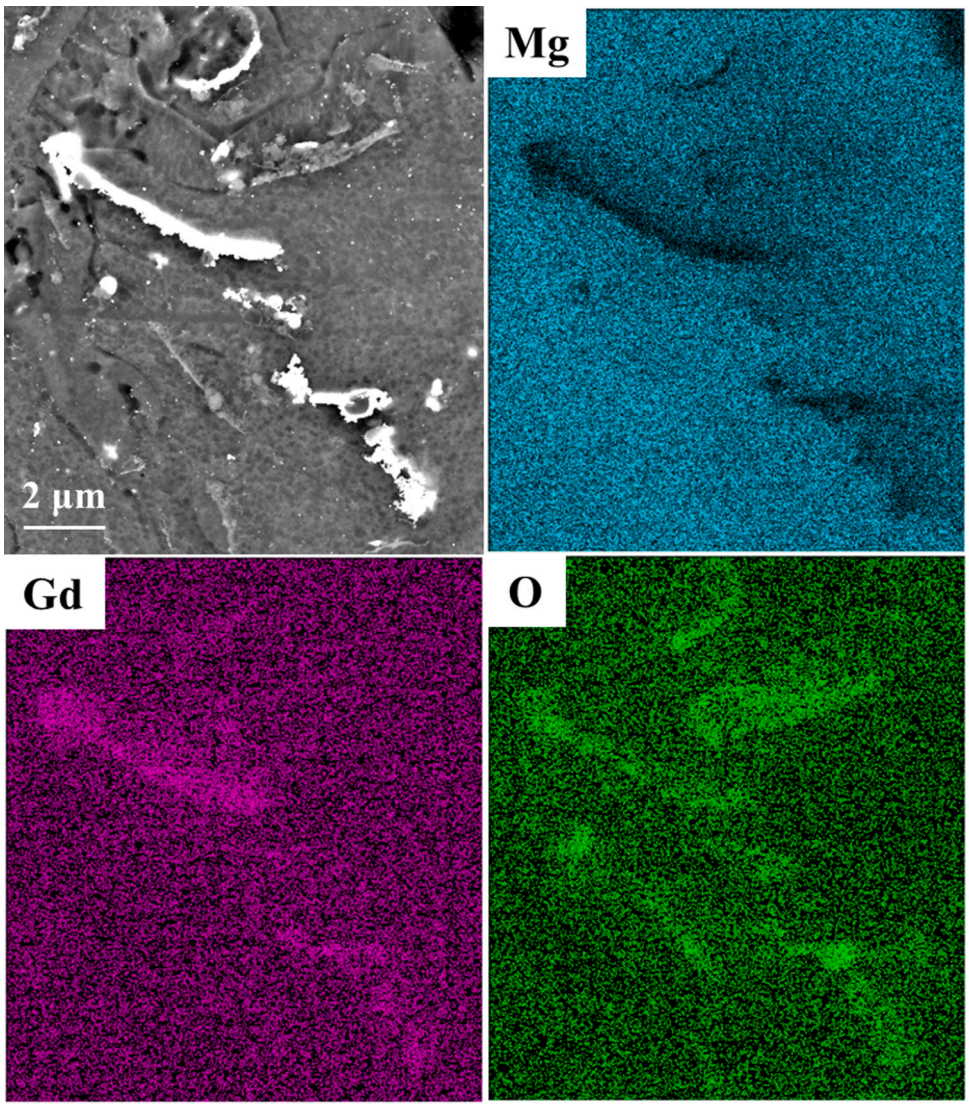

Fig. 6. BSE-SEM micrographs and corresponding EDS maps of oxide particles in the SLMed G10K alloy.

grains in the SLMed and FSPed G10K alloys. Fig. 7 presents the EBSD orientation map (a, c) and grain size distribution (b, d) of the SLMed (a, b) and FSPed (c, d) G10K alloys. The SLMed G10K alloy mainly consists of columnar grains with a typical width of about 30 μm and a representative height of about 100 μm, which grow along the BD of SLM process. The formation of columnar grains should be attributed to the next two aspects: firstly, the large temperature gradient provides favorable conditions for the development of columnar grains; secondly, the relatively low content of Zr element compared with as-cast Mg alloys leads to a lower Q value of growth restriction factor [35], which cannot provide sufficient constitutional supercooling and heterogeneous nucleation cores during solidification. Apart from coarse columnar grains, there are a few equiaxed grains distributed near the boundary of the molten pool with an area fraction of 27.45%. The coarse columnar grains in the SLMed alloy are successfully broken down due to the complex deformation under the shoulder and around the pin. The average grain size was also notably refined from 26.85 ± 15.43 μm to 5.78 ± 2.25 μm owing to dynamic recrystallization (DRX) phenomenon during FSP process. The standard deviation of the average grain size of the SLMed alloy is much higher than that of the FSPed alloy because of mixed distribution of columnar and equiaxed grains.

3.3. The influence of FSP on aging precipitates

Fig. 8 exhibits the aging hardening curves of the SLMed and FSPed G10K alloys at temperature of 200°C. Table 2 lists the crucial characteristics of the aging hardening curves. Both the SLMed and FSPed alloys share similar aging hardening features, achieving the peak-aged hardness at 32 h. FSP can not only increase the initial hardness (from 79.8 HV to 86.2 HV) owing to the refined and homogenized microstructure, but also increase the peak-aged hardness (from 102.5 HV to 114.5 HV). Besides, the aging hardening response (hardness increment 28.3 HV versus 22.7 HV) is enhanced after FSP, a 25% increase has been achieved. One of the reasons for this is the dissolution of the eutectic phase during FSP increasing the supersaturation degree of Gd element. Other reasons will be discussed according to below TEM micrographs of precipitates.

Fig. 9 shows bright-field (BF) TEM micrographs (a, c) and corresponding selected area electron diffraction (SAED) patterns (b, d) of the α-Mg matrix and β' aging precipitates in the SLM-T5 G10K alloy, where the white arrows in Fig. 9a and c indicate the representative β' precipitates. The extra weak diffraction spots in the SAED patterns (Fig. 9b, d) comes from the prismatic β′ metastable phases with cbco structure (a = 0.650 nm , b = 2.272 nm , c = 0.521 nm), which are the foremost and effective strengthening phases in Mg-Gd series alloys [26,34,36]. As

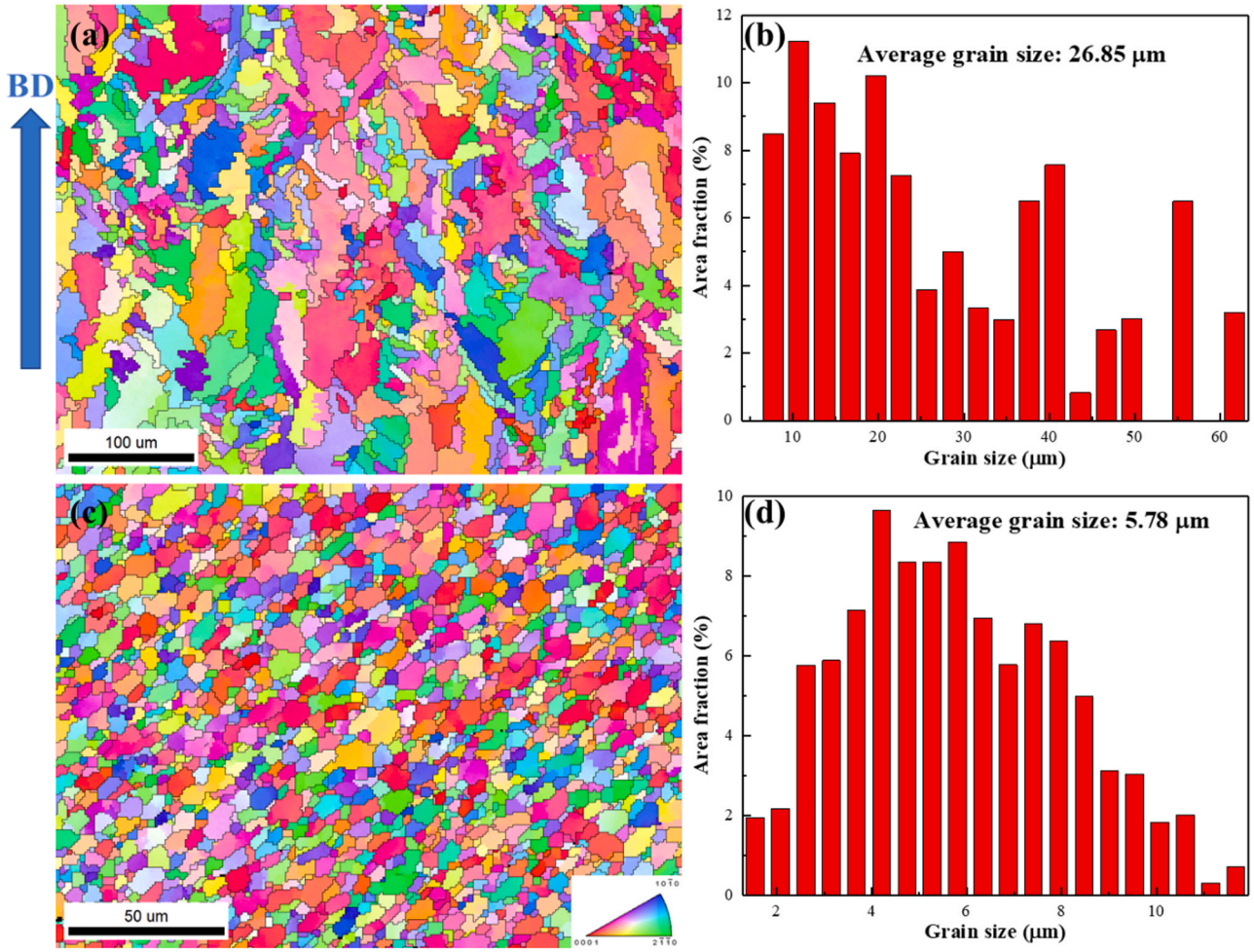

Fig. 7. The EBSD orientation map (a, c) and grain size distribution (b, d) of SLMed (a, b) and FSPed (c, d) G10K alloy.

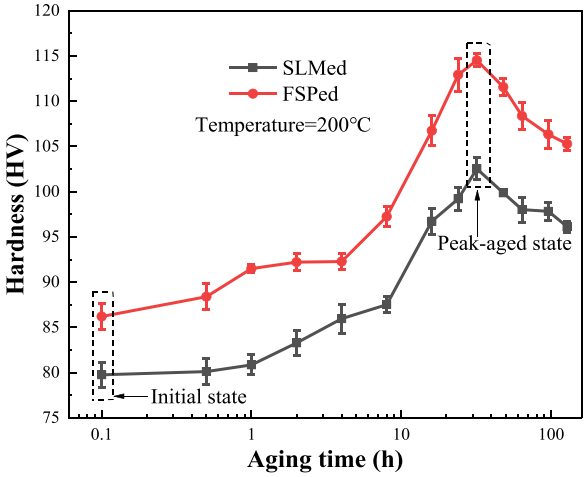

Fig. 8. The aging hardening curves of the SLMed and FSPed G10K alloy.

shown in Fig. 9c, dense β' aging precipitates are evenly spreaded in the α-Mg matrix, which are the most valid barrier to dislocation slip and twin propagation in the α-Mg matrix [37].

Fig. 10 presents BF TEM micrographs (a, c) and corresponding SAED patterns (b, d) of the α-Mg matrix and β' aging precipitates in the FSP-T5 G10K alloy. Evenly distributed dense prismatic β' precipitates also exist in the FSP-T5 G10K alloy (Fig. 10a and c). Thus, FSP will not change the

Table 2
The crucial characteristics of the ageing hardening curves of the SLMed and FSPed G10K alloy at temperature of 200°C.

Initial state	Initial hardness/HV	Peak-aged hardness/HV	Hardness increment/HV	Time to peak-aged hardness/h
SLM	79.8 ± 1.4	102.5 ± 1.2	22.7	32
FSP	86.2 ± 1.5	114.5 ± 0.7	28.3	32

types of aging precipitates in the aging heat treatment process. However, the diffraction spots (Fig. 10b and d) of β' precipitates in the FSP-T5 G10K alloy are clearer and stronger than those in the SLM-T5 G10K alloy, indicating a higher content of β' precipitates in the FSP-T5 G10K alloy.

The area number density of β' aging precipitates is defined as the amount of precipitates per unit area. The size of the plate-shaped precipitates includes length along the direction of $\left[01\bar{1}0\right]_{\alpha}$, width along the direction of $\left[11\bar{2}0\right]_{\alpha}$, height along the direction of $[0001]_{\alpha}$. By counting more than 10 TEM images including over 200 β' precipitates, the average area number density and size of the β' precipitates in the SLM-T5 and FSP-T5 G10K alloys are enumerated in Table 3. The height of the β' precipitates increases obviously from 9.05 nm to 17.42 nm while the length and width are slightly reduced from 7.70 nm, 5.00 nm to 6.76 nm, 4.70 nm respectively after FSP. In other words, FSP can change the morphology of the β' precipitates. Nie et al. [38] reported that the YS

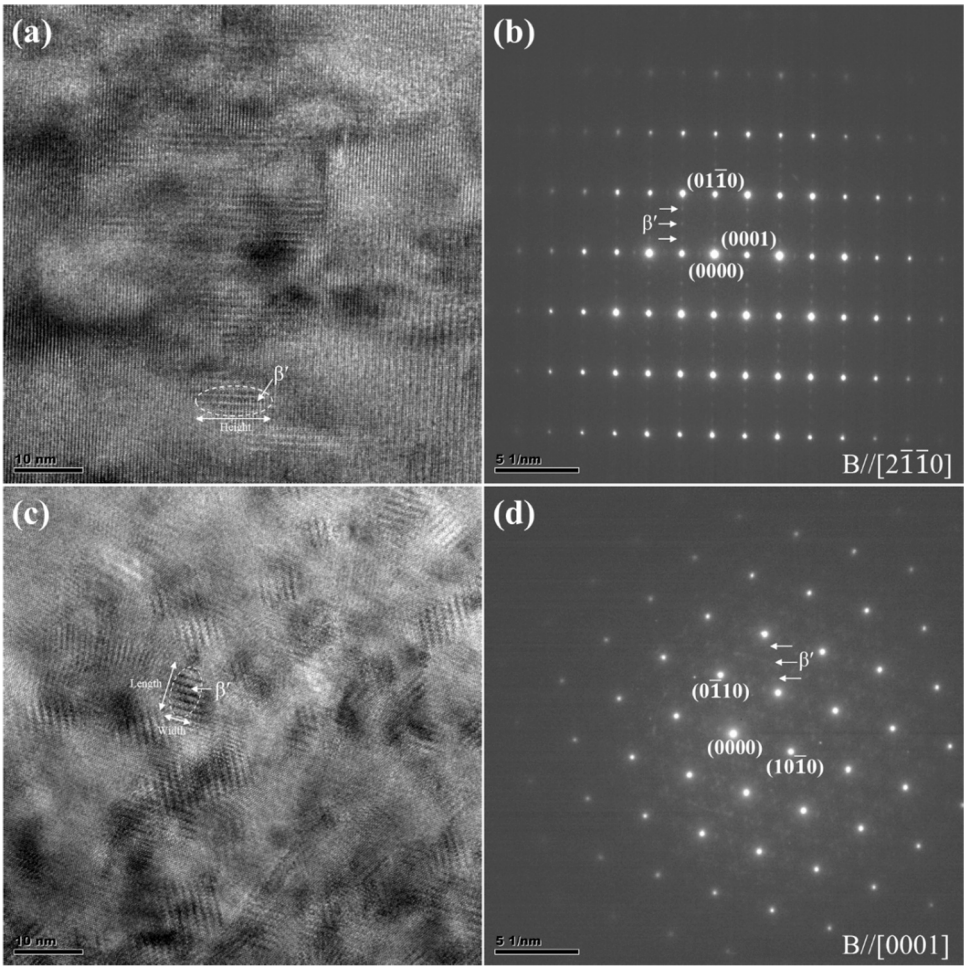

Fig. 9. BF TEM micrographs (a, c) and corresponding SAED patterns (b, d) of the β' precipitates in the SLM-T5 G10K alloy. The beams were parallel to the $\left[2\bar{1}\bar{1}0\right]_{\alpha}$ direction in (a) and the $[0001]_{\alpha}$ direction in (c).

increment originating from the prismatic β' precipitates increases significantly with the increase of plate aspect ratio (height divided by width). Therefore, changes in the morphology of the β' precipitates after FSP cause the plate aspect ratio to increase from 1.81 to 3.71 (almost twice), which will provide more strengthening effects. Moreover, the area number density of the β' precipitates increases from 3.57×10^{-3} nm^{-2} to 5.20×10^{-3} nm^{-2}, indicating a 46% increase. Higher area number density of the β' precipitates contributes to stronger ageing hardening response (Table 2) in the FSPed G10K alloy because ageing hardening response is tightly associated with the density of precipitates. Heng et al. [39] found that the strain before aging heat treatment promotes the precipitation of precipitates due to the higher dislocation density introduced by deformation. Crystal defects like lattice distortion and dislocations will be imparted into the alloy after FSP, which will provide the heterogeneous nucleation sites for precipitates during subsequent aging heat treatment [37]. Therefore, FSP can increase the plate aspect ratio and area number density of the β' precipitates significantly resulting in stronger aging hardening response.

Fig. 11 illustrates the schematic diagram illustrating the microstructural characteristics of the G10K alloys under the SLM, FSP, SLM-T5 and FSP-T5 conditions. In summary, FSP can eliminate pores and molten pool boundary, promote the transformation of columnar grains to equiaxed grains and refine grains. After aging heat treatment, compared with SLM-T5 G10K alloy, the height of β' precipitates is significantly increased while the length is slightly reduced resulting in a significantly increased plate aspect ratio of β' precipitates in FSP-T5 G10K alloy.

3.4. The influence of FSP on mechanical properties

Fig. 12 presents representative engineering stress-strain curves and room temperature tensile properties of the G10K alloys under the SLM, FSP, SLM-T5 and FSP-T5 conditions. The YS, UTS and EL of the FSPed G10K alloy are 202 ± 5 MPa, 272 ± 10 MPa and $7.5 \pm 0.5\%$ respectively. As a comparison, the YS, UTS and EL of the SLMed G10K alloy are only 180 ± 6 MPa, 228 ± 9 MPa and $2.2 \pm 0.3\%$ respectively. Therefore, FSP can improve tensile strength and ductility simultaneously, especially the EL is greatly increased from 2.2% to 7.5%, indicating a 241% increase. After aging heat treatment, the tensile strength is remarkably improved but the ductility is also significantly reduced because of the dense precipitates. Especially, compared with the FSPed G10K alloy, the YS and UTS of the FSP-T5 G10K alloy increase by 83 MPa and 84 MPa respectively, while the increments are only 63 MPa and 32 MPa in the SLM-T5 G10K alloy. This is consistent with the larger increment in hardness of FSP-T5 G10K alloy. The FSP-T5 G10K alloy exhibits the highest tensile strength: YS is 285 ± 7 MPa, UTS is 356 ± 8 MPa while the EL is only $1.3 \pm 0.2\%$.

Fig. 13 shows the room temperature tensile fracture morphologies of the G10K alloys under the SLM, FSP, SLM-T5 and FSP-T5 conditions. There are many pores (orange arrows) in the fracture of the SLMed alloy at low magnification (Fig. 13a), which causes premature fracture during the tensile test. The other area of the fracture is composed of a large amount of cleavage planes (white arrows) and a small number of dimples (yellow arrows) (Fig. 13b). The fracture becomes very dense after FSP, with almost no pores (Fig. 13c). The fracture of the FSPed alloy is

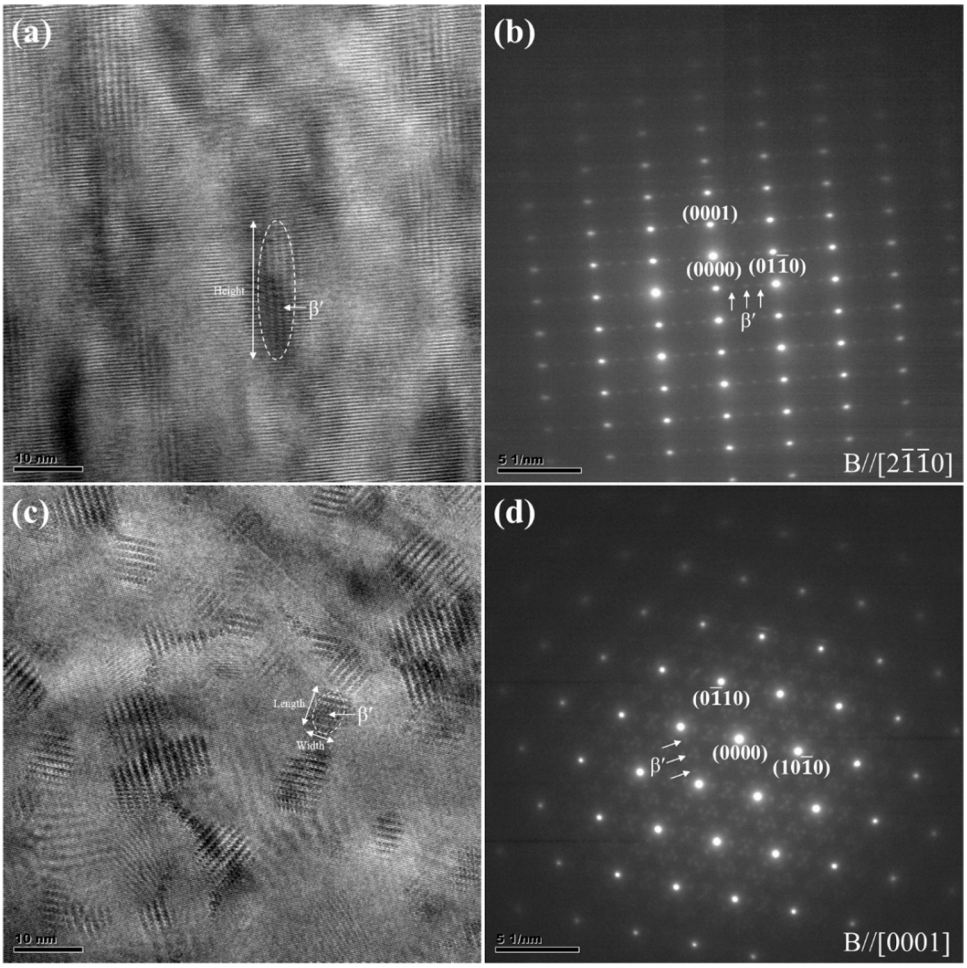

Fig. 10. BF TEM micrographs (a, c) and corresponding SAED patterns (b, d) of the β' precipitates in the FSP-T5 G10K alloy. The beams were parallel to the $\left[2\bar{1}\bar{1}0\right]_{\alpha}$ direction in (a) and the $[0001]_{\alpha}$ direction in (c).

Table 3
Area number density and size of the β' precipitates in the SLM-T5 and FSP-T5 G10K alloys.

State	Area number density/ 10^{-3} nm^{-2}	Length/nm	Width/nm	Height/nm
SLM-T5	3.57 ± 0.44	7.70 ± 1.33	5.00 ± 0.87	9.05 ± 1.71
FSP-T5	5.20 ± 0.37	6.76 ± 1.75	4.70 ± 1.24	17.42 ± 2.52

composed of numerous extremely small dimples of 500 nm in diameter with a small amount of cleavage planes (Fig. 13d), implying the feature of ductile-brittle hybrid fracture. Therefore, the FSP alloy obtains excellent EL of 7.5%. After aging heat treatment, many pores do not change (Fig. 13e) but the cleavage planes become larger and there are almost no dimples (Fig. 13f), resulting in a significant drop in EL of SLM-T5 alloy. As for the FSP-T5 alloy, the fracture mainly includes cleavage planes and the number of dimples is reduced (Fig. 13g and h) compared with the FSP alloy, so the EL is obviously declined after aging heat treatment.

It is well accepted that the ductile fracture contains three stages: void nucleation, growth and coalescence [40]. The low EL of the SLMed G10K alloy is mostly due to the following reasons: (i) the existence of many large pores; (ii) the existence of oxide particles; (iii) inhomogeneous microstructure including coarse columnar grains and equiaxed grains; (iv) residual stress [16]. In the case of the SLMed G10K alloy, the initiation and propagation of cracks occurs in advance, as pre-existing pores grow straightly with the successive stretch deformation, and then merge with newly nucleated voids or other grown pores. However, the closure of pores, the reduction and refinement of oxide particles, uniform microstructure consisting of fully fine equiaxed grains and the relief of residual stress, all of the above contribute to a significant increase in EL after FSP. As for the improvement of YS, the significant fine grain strengthening derived from fully fine equiaxed grains and dispersion strengthening originated from fine dot-like Mg_5Gd phases although the dissolution of the eutectic phase results in small loss of strength. Both improved work hardening effect brought by the enhancement of EL and the increase in YS contribute to the improvement of UTS of the FSPed G10K alloy compared with the SLMed G10K alloy. After aging heat treatment, higher plate aspect ratio and area number density of the β' precipitates in FSP-T5 G10K alloy compared with the SLM-T5 G10K alloy lead to higher YS increment. The EL of SLM-T5 G10K alloy and FSP-T5 G10K alloy are distinctly reduced after aging heat treatment. The higher EL of the FSP-T5 G10K alloy is inherited from FSP state.

Table 4 lists room temperature tensile properties of Mg alloys under SLM state and post treatment state in literature and present work. Firstly, the YS, UTS and EL of the FSPed G10K alloy are superior to those of the SLMed G10K alloy especially EL. Secondly, the YS, UTS and EL of the FSP-T5 G10K alloy are also superior to those of the SLM-T5 G10K alloy. As a comparison, HIP of SLMed AZ61 Mg alloy can increase EL obviously due to the reduction of porosity and the dissolution of hard-brittle β-$Mg_{17}Al_{12}$ phase while YS decreases dramatically at the same

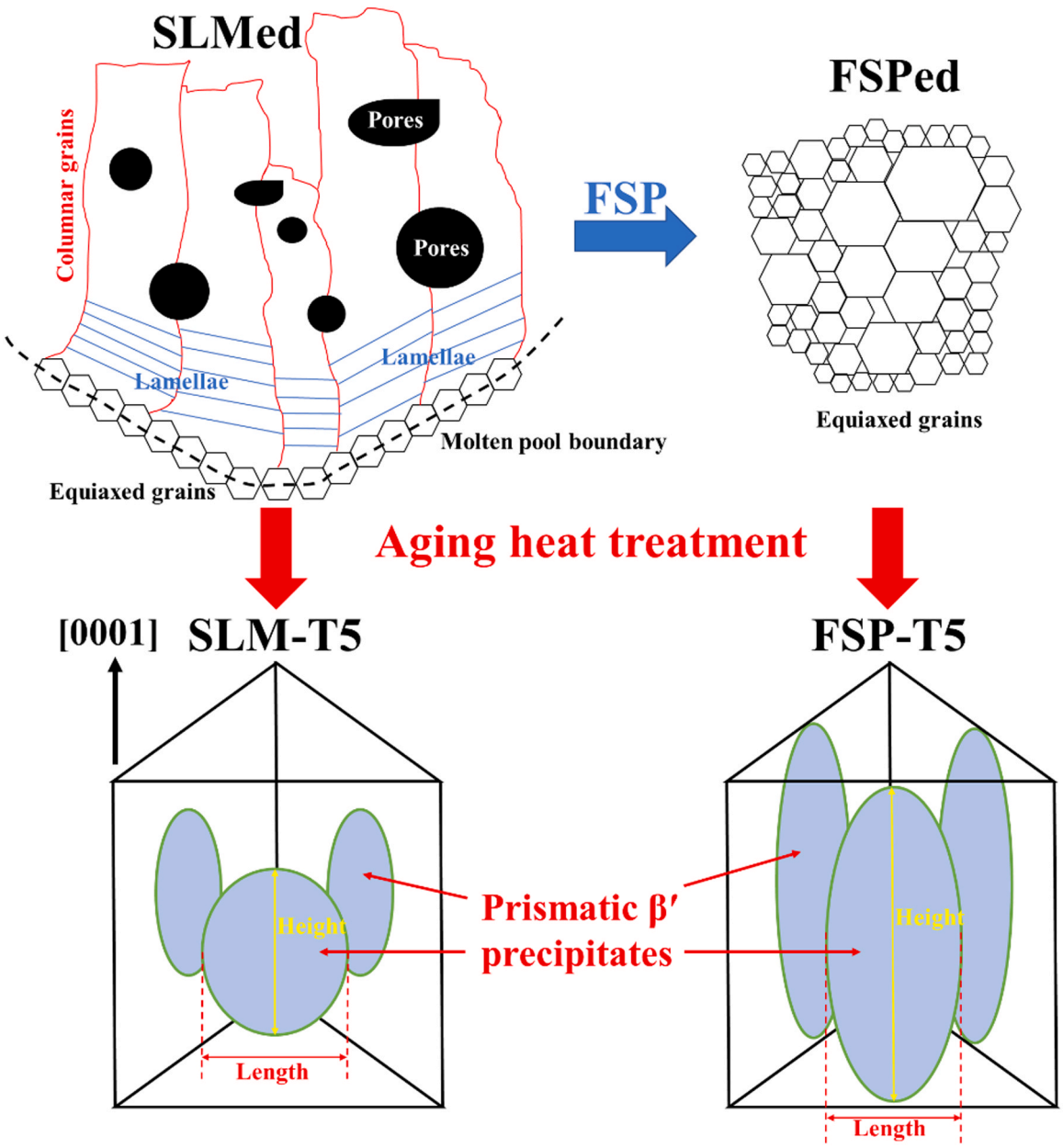

Fig. 11. The schematic diagram illustrating the microstructural characteristics of the G10K alloys under the SLM, FSP, SLM-T5 and FSP-T5 conditions.

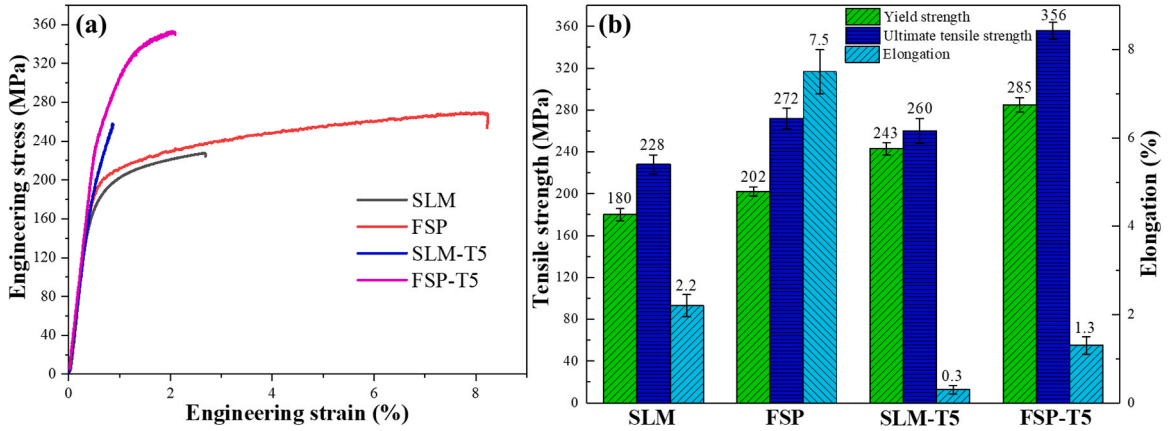

Fig. 12. Representative tensile engineering stress-strain curves (a) and room temperature tensile properties (b) of the G10K alloys under the SLM, FSP, SLM-T5 and FSP-T5 conditions.

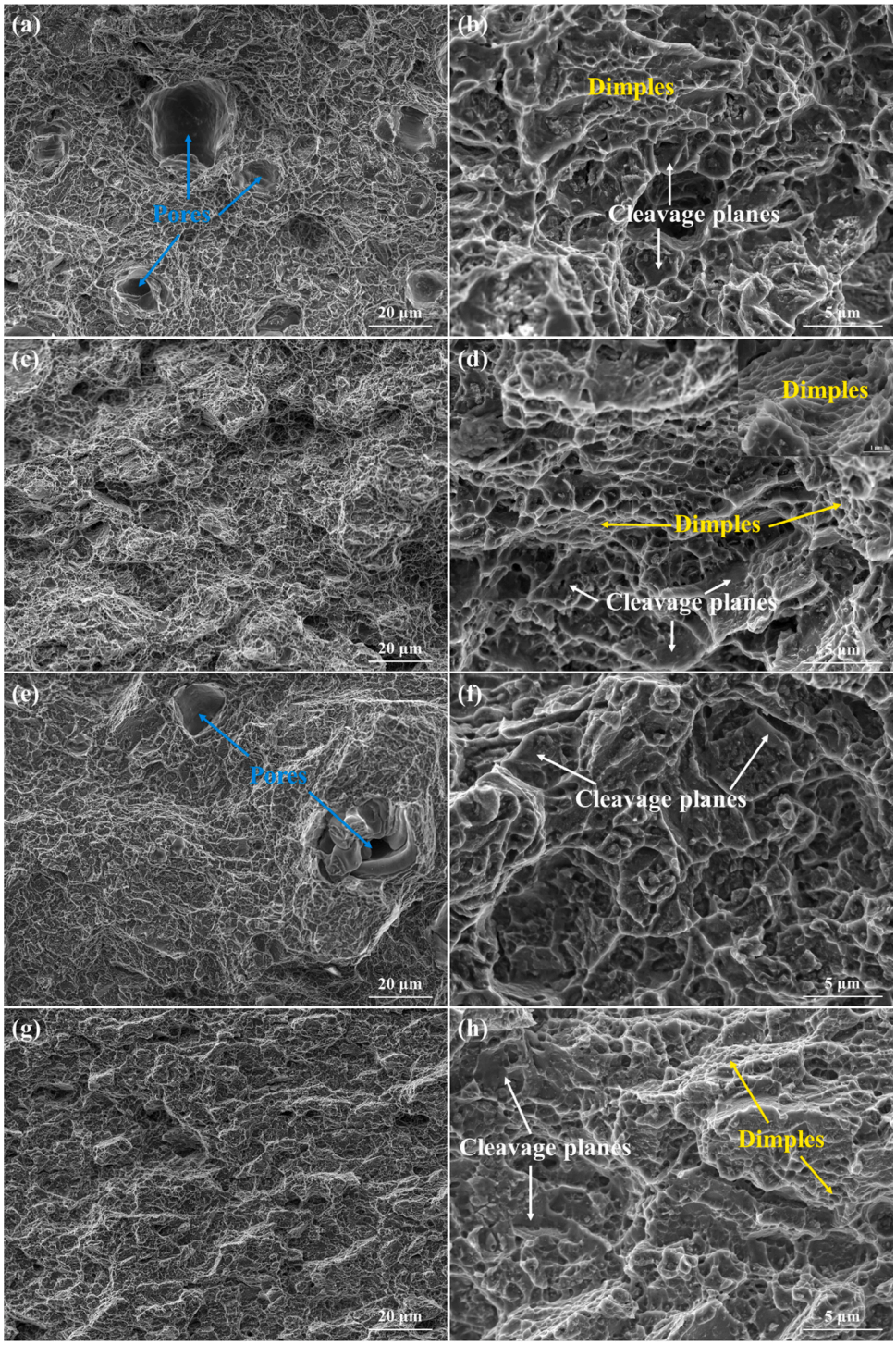

Fig. 13. The room temperature tensile fracture morphologies of the G10K alloys under the SLM (a, b), FSP (c, d), SLM-T5 (e, f) and FSP-T5 (g, h) conditions.

time as a result of the growth of grain size from 2.2 μm in SLM state to 23.9 μm in HIP state [19]. As for traditional T6 heat treatment designed for as-cast alloys, a small increase in EL compared with SLM state is achieved while YS and UTS remain basically unchanged. This should be attributed to offset of grain growth weakening effect after solution heat treatment and plate-like β_1-Mg_3Nd precipitate strengthening effect after subsequent age hardening in WE43 Mg alloy [13]. In summary, FSP is a very effective for enhancing room temperature tensile properties of the SLMed alloys. Significant improvement of tensile strength and EL is achieved after FSP of the SLMed G10K alloy.

4. Conclusions

A SLMed G10K Mg alloy has been successfully modified by FSP in this study. Detailed analysis of the influence of FSP on pore defects, molten pool boundary, grain morphology, aging precipitates and mechanical properties provide the following conclusions:

(1) FSP leads to porosity reduction from 0.779% to 0.015%, vanishment of molten pool boundaries, columnar to equiaxed transition and grain refinement from 26.85 μm to 5.78 μm, thus

Table 4
Room temperature tensile properties of Mg alloys under SLM state and post treatment state.

Alloys	States	UTS/MPa	YS/MPa	EL/%	Reference
AZ61	SLM	287	274	3.1	[12,19]
	HIP	233	126	8.2	
WE43	SLM	251	215	2.6	[13]
	SLM-T6	251	219	4.3	
G10K	SLM	228	180	2.2	Present work
	FSP	272	202	7.5	
	SLM-T5	260	243	0.3	
	FSP-T5	356	285	1.3	

bringing a homogenization effect on the mesoscopic and micro structural scale.

(2) FSP can not only modify the morphology of the β' aging precipitates with a larger plate aspect ratio, but also increase the area number density of the β' precipitates, both of which result in stronger aging hardening response of FSP-T5 G10K alloy.

(3) FSP can improve room temperature tensile properties significantly. Both tensile strength (YS and UTS) and ductility (EL) of the FSPed and FSP-T5 G10K alloys are quite superior to those of the SLMed and SLM-T5 G10K alloys. The FSPed and FSP-T5 G10K alloys exhibit YS of 202 and 285 MPa, UTS of 272 and 356 MPa, EL of 7.5% and 1.3% respectively.

CRediT authorship contribution statement

Qingchen Deng: Conceptualization, Methodology, Investigation, Writing - original draft, Writing - review & editing. **Yujuan Wu:** Writing - review & editing, Validation, Supervision, Funding acquisition. **Ning Su:** Writing - review & editing. **Zhiyu Chang:** Writing - review & editing. **Juan Chen:** Writing - review & editing, Supervision. **Liming Peng:** Supervision, Funding acquisition, Resources, Project administration. **Wenjiang Ding:** Supervision, Funding acquisition, Resources.

Declaration of Competing Interest

The authors declare that they have no known competing financial interests or personal relationships that could have appeared to influence the work reported in this paper.

Acknowledgment

This work was funded by the National Natural Science Foundation of China (Nos. 51971130, 51771113, 51821001) and High Technology and Key Development Project of Ningbo, China (No. 2019B10102). Thanks to the support of Tangshan Weihao Magnesium Powder Co., LTD. for producing the alloy powders.

References

[1] W. Zhang, L. Wang, Z. Feng, Y. Chen, Research progress on selective laser melting (SLM) of magnesium alloys: a review, Optik 207 (2020), 163842.
[2] S. Liu, H. Guo, A review of SLMed magnesium alloys: processing, properties, alloying elements and postprocessing, Metals 10 (2020) 1073.
[3] R. Karunakaran, S. Ortgies, A. Tamayol, F. Bobaru, M.P. Sealy, Additive manufacturing of magnesium alloys, Bioact. Mater. 5 (2020) 44–54.
[4] Y. Yang, C. He, E. Dianyu, W. Yang, F. Qi, D. Xie, L. Shen, S. Peng, C. Shuai, Mg bone implant: features, developments and perspectives, Mater. Des. 185 (2020), 108259.
[5] T. Kurzynowski, A. Pawlak, I. Smolina, The potential of SLM technology for processing magnesium alloys in aerospace industry, Arch. Civ. Mech. Eng. 20 (2020) 23.
[6] Y. Yang, Y. Cheng, S. Peng, L. Xu, C. He, F. Qi, M. Zhao, C. Shuai, Microstructure evolution and texture tailoring of reduced graphene oxide reinforced Zn scaffold, Bioact. Mater. 6 (2021) 1230–1241.
[7] J. Song, J. She, D. Chen, F. Pan, Latest research advances on magnesium and magnesium alloys worldwide, J. Magnes. Alloy. 8 (2020) 1–41.
[8] K.G. Prashanth, S. Scudino, H.J. Klauss, K.B. Surreddi, L. Löber, Z. Wang, A. K. Chaubey, U. Kühn, J. Eckert, Microstructure and mechanical properties of Al–12Si produced by selective laser melting: Effect of heat treatment, Mater. Sci. Eng.: A 590 (2014) 153–160.
[9] Q. Deng, Y. Wu, Y. Luo, N. Su, X. Xue, Z. Chang, Q. Wu, Y. Xue, L. Peng, Fabrication of high-strength Mg-Gd-Zn-Zr alloy via selective laser melting, Mater. Charact. 165 (2020), 110377.
[10] N.A. Zumdick, L. Jauer, L.C. Kersting, T.N. Kutz, J.H. Schleifenbaum, D. Zander, Additive manufactured WE43 magnesium: a comparative study of the microstructure and mechanical properties with those of powder extruded and as-cast WE43, Mater. Charact. 147 (2019) 384–397.
[11] K. Wei, M. Gao, Z. Wang, X. Zeng, Effect of energy input on formability, microstructure and mechanical properties of selective laser melted AZ91D magnesium alloy, Mater. Sci. Eng. A 611 (2014) 212–222.
[12] S. Liu, W. Yang, X. Shi, B. Li, S. Duan, H. Guo, J. Guo, Influence of laser process parameters on the densification, microstructure, and mechanical properties of a selective laser melted AZ61 magnesium alloy, J. Alloy. Compd. 808 (2019), 151160.
[13] H. Hyer, L. Zhou, G. Benson, B. McWilliams, K. Cho, Y. Sohn, Additive manufacturing of dense WE43 Mg alloy by laser powder bed fusion, Addit. Manuf. 33 (2020), 101123.
[14] W. Liu, C. Chen, S. Shuai, R. Zhao, L. Liu, X. Wang, T. Hu, W. Xuan, C. Li, J. Yu, J. Wang, Z. Ren, Study of pore defect and mechanical properties in selective laser melted Ti6Al4V alloy based on X-ray computed tomography, Mater. Sci. Eng. A 797 (2020), 139981.
[15] J.G. Santos Macías, C. Elangeswaran, L. Zhao, B. Van Hooreweder, J. Adrien, E. Maire, J.-Y. Buffière, W. Ludwig, P.J. Jacques, A. Simar, Ductilisation and fatigue life enhancement of selective laser melted AlSi10Mg by friction stir processing, Scr. Mater. 170 (2019) 124–128.
[16] J.L. Bartlett, X. Li, An overview of residual stresses in metal powder bed fusion, Addit. Manuf. 27 (2019) 131–149.
[17] V. Manakari, G. Parande, M. Gupta, Selective laser melting of magnesium and magnesium alloy powders: a review, Metals 7 (2016) 1–35.
[18] V. Chastand, P. Quaegebeur, W. Maia, E. Charkaluk, Comparative study of fatigue properties of Ti-6Al-4V specimens built by electron beam melting (EBM) and selective laser melting (SLM), Mater. Charact. 143 (2018) 76–81.
[19] S. Liu, H. Guo, Influence of hot isostatic pressing (HIP) on mechanical properties of magnesium alloy produced by selective laser melting (SLM), Mater. Lett. 265 (2020), 127463.
[20] Q. Tan, J. Zhang, Q. Sun, Z. Fan, G. Li, Y. Yin, Y. Liu, M.-X. Zhang, Inoculation treatment of an additively manufactured 2024 aluminium alloy with titanium nanoparticles, Acta Mater. 196 (2020) 1–16.
[21] J. Han, J. Chen, L. Peng, S. Tan, Y. Wu, F. Zheng, H. Yi, Microstructure, texture and mechanical properties of friction stir processed Mg-14Gd alloys, Mater. Des. 130 (2017) 90–102.
[22] X.C. Luo, L.M. Kang, H.L. Liu, Z.J. Li, Y.F. Liu, D.T. Zhang, D.L. Chen, Enhancing mechanical properties of AZ61 magnesium alloy via friction stir processing: Effect of processing parameters, Mater. Sci. Eng.: A 797 (2020), 139945.
[23] B. Li, X. Hou, B. Teng, Effects of friction stir process and subsequent aging treatment on the microstructure evolution and mechanical properties of Mg-Gd-Y-Zn-Zr alloy, Mater. Charact. 155 (2019), 109832.
[24] X.W. Li, F.Y. Zheng, Y.J. Wu, L.M. Peng, Y. Zhang, D.L. Lin, W.J. Ding, Modification of long period stacking ordered phase and improvement of mechanical properties of Mg–Gd–Zn–Zr alloy by friction stir processing, Mater. Lett. 113 (2013) 206–209.
[25] C. Huang, X. Yan, L. Zhao, M. Liu, W. Ma, W. Wang, J. Soete, A. Simar, Ductilization of selective laser melted Ti6Al4V alloy by friction stir processing, Mater. Sci. Eng.: A 755 (2019) 85–96.
[26] Y. Zhang, W. Rong, Y. Wu, L. Peng, J.-F. Nie, N. Birbilis, A detailed HAADF-STEM study of precipitate evolution in Mg–Gd alloy, J. Alloy. Compd. 777 (2019) 531–543.
[27] N. Su, X. Xue, H. Zhou, Y. Wu, Q. Deng, K. Yang, Q. Chen, B. Chen, L. Peng, Effects of nanoprecipitates and LPSO structure on deformation and fracture behaviour of high-strength Mg-Gd-Y-Zn-Mn alloys, Mater. Charact. 165 (2020), 110396.
[28] S. Ning, W. Yujuan, C. Zhiyu, D. Qingchen, P. Liming, Y. Kun, C. Qiang, Selective variant growth of precipitates in an as-extruded Mg-Gd-Zn-Mn alloy, Mater. Lett. 272 (2020), 127853.
[29] F. Hannard, S. Castin, E. Maire, R. Mokso, T. Pardoen, A. Simar, Ductilization of aluminium alloy 6056 by friction stir processing, Acta Mater. 130 (2017) 121–136.
[30] X. Niu, H. Shen, J. Fu, Microstructure and mechanical properties of selective laser melted Mg-9wt%Al powder mixture, Mater. Lett. 221 (2018) 4–7.
[31] F. Bar, L. Berger, L. Jauer, G. Kurtuldu, R. Schaublin, J.H. Schleifenbaum, J. F. Loffler, Laser additive manufacturing of biodegradable magnesium alloy WE43: a detailed microstructure analysis, Acta Biomater. 98 (2019) 36–49.
[32] D. Wang, P. Fu, L. Peng, Y. Wang, W. Ding, A study of microstructure, mechanical behavior and strengthen mechanism in the Mg-10Gd-0.2Zn-(Y)-0.4Zr alloy, Mater. Sci. Eng. A 793 (2020), 139881.
[33] L. Xiao, G. Yang, J. Ma, H. Qin, J. Li, W. Jie, Microstructure evolution and fracture behavior of Mg-9.5Gd-0.9Zn-0.5Zr alloy subjected to different heat treatments, Mater. Charact. 168 (2020), 110516.
[34] W. Rong, Y. Wu, Y. Zhang, M. Sun, J. Chen, L. Peng, W. Ding, Characterization and strengthening effects of γ′ precipitates in a high-strength casting Mg-15Gd-1Zn-0.4Zr (wt%) alloy, Mater. Charact. 126 (2017) 1–9.
[35] D.H. StJohn, M. Qian, M.A. Easton, P. Cao, The Interdependence Theory: The relationship between grain formation and nucleant selection, Acta Mater. 59 (2011) 4907–4921.

[36] D. Wang, P. Fu, L. Peng, Y. Wang, W. Ding, Development of high strength sand cast Mg–Gd–Zn alloy by co-precipitation of the prismatic β′ and β1 phases, Mater. Charact. 153 (2019) 157–168.
[37] J.F. Nie, Precipitation and hardening in magnesium alloys, Metall. Mater. Trans. A 43 (2012) 3891–3939.
[38] J.F. Nie, Effects of precipitate shape and orientation on dispersion strengthening in magnesium alloys, Scr. Mater. 48 (2003) 1009–1015.
[39] X. Heng, Y. Zhang, W. Rong, Y. Wu, L. Peng, A super high-strength Mg-Gd-Y-Zn-Mn alloy fabricated by hot extrusion and strain aging, Mater. Des. 169 (2019), 107666.
[40] U.M. Chaudry, K. Hamad, J.G. Kim, On the ductility of magnesium based materials: a mini review, J. Alloy. Compd. 792 (2019) 652–664.